Mon. Not. R. Astron. Soc. **000**, 000–000 (0000) Printed 27 June 2013 (MN LATEX style file v2.2)

The imprint of the crustal magnetic field on the thermal spectra and pulse profiles of isolated neutron stars

Rosalba Perna[1], Daniele Viganò[2], José A. Pons[2], Nanda Rea[3]
[1] *Department of Astrophysical and Planetary Sciences and JILA, University of Colorado, 440 UCB, Boulder, 80309, USA*
[2] *Departament de Física Aplicada, Universitat d'Alacant, Ap. Correus 99, 03080 Alacant, Spain*
[3] *Institute of Space Sciences (CSIC–IEEC), Campus UAB, Faculty of Science, Torre C5-parell, E-08193 Barcelona, Spain*

ABSTRACT

Isolated neutron stars (NSs) show a bewildering variety of astrophysical manifestations, presumably shaped by the magnetic field strength and topology at birth. Here, using state-of-the art calculations of the coupled magnetic and thermal evolution of NSs, we compute the thermal spectra and pulse profiles expected for a variety of initial magnetic field configurations. In particular, we contrast models with purely poloidal magnetic fields to models dominated by a strong internal toroidal component. We find that, while the former displays double peaked profiles and very low pulsed fractions, in the latter, the anisotropy in the surface temperature produced by the toroidal field often results in a single pulse profile, with pulsed fractions that can exceed the $50-60\%$ level even for perfectly isotropic local emission. We further use our theoretical results to generate simulated "observed" spectra, and show that blackbody (BB) fits result in inferred radii that can be significantly smaller than the actual NS radius, even as low as $\sim 1-2$ km for old NSs with strong internal toroidal fields and a high absorption column density along their line of sight. We compute the size of the inferred BB radius for a few representative magnetic field configurations, NS ages, and magnitudes of the column density. Our theoretical results are of direct relevance to the interpretation of X-ray observations of isolated NSs, as well as to the constraints on the equation of state of dense matter through radius measurements.

1 INTRODUCTION

Observations of isolated neutron stars (NSs) over the last several decades have painted a zoo of disparate manifestations, in energy bands ranging from the gamma-rays to the radio. The bulk of isolated NSs manifest themselves as radio pulsars and are characterized by a rather steady spin down. These NSs have an estimated magnetic field in the $\sim 10^{12}-10^{13}$ G range. A fraction of NSs are further characterized by large surface temperatures for their ages, occasional X-ray bursts, and, in some cases, even giant γ-ray flares. These objects, historically classified as Anomalous X-ray Pulsars (AXPs) and Soft γ-ray Repeaters (SGRs), and collectively known as magnetars, have very large estimated magnetic field strengths, $\sim 10^{14}-10^{15}$ G. The large fields are believed to be responsible for their observational characteristics (Thompson & Duncan 1995).

Other NSs, at the opposite end of the spectrum, are very quiet and their surface emission is generally consistent with thermal emission from the entire surface of the star. These objects, also known as Central Compact Objects (CCOs), have been proposed to be NSs with very low external magnetic field strengths, $B \lesssim 10^{11}$ G, either by birth (Gotthelf & Halpern 2009), or as the result of field screening by fallback accreted matter (Muslimov & Page 1995; Young & Chanmugam 1995; Bernal et al. 2010; Ho 2011; Viganò & Pons 2012).

Evidently, the magnetic field strength of a NS plays a fundamental role in its observational appearance and in its evolutionary path. Indeed, a large number of investigations over several decades have been aimed at understanding how the B-field shapes the NS life and properties as we see them (e.g. Heyl & Kulkarni 1998). Clearly, the dipolar field component, inferred through measurements of P and $\dot{P}$, is not sufficient to account for this variety of behaviours, calling for a re-evaluation of our global understanding of the relation between the inferred B-field and the phenomenology of a NS. As discussed in a series of previous papers (Pons et al. 2007; Aguilera et al. 2008; Pons et al. 2009; Viganò et al. 2013), magnetic and thermal evolution are strongly coupled. The standard, 1D cooling theory is able to predict the range of observed temperatures and luminosities for weakly magnetised objects. However, under the presence of a strong magnetic field, two other important effects play a role in influencing the observational properties of the NSs: the gradual conversion of magnetic energy into heat via the Joule effect in the crust, and the anisotropy in the surface temperature distribution.

For strongly magnetised NSs ($B \gtrsim 10^{14}$ G), the dissipation of currents circulating in the crust maintains the

crust at high temperatures ($T_c \gtrsim 10^8$ K) and consequently the average surface temperature is also higher than in the non-magnetic case. The first consequence is an enhancement of the persistent luminosity: the most magnetized objects (magnetars, high-B pulsars) are systematically brighter, and they are much easier to detect than the weakly magnetised ones. The second important effect, on which we focus in this work, is the anisotropy in temperature induced by the magnetic field. Under the presence of a strong field, the conductivity becomes anisotropic, due to the fact that the electrons, which are the main responsible for the heat transport, move more easily along the field lines than across them. In the outer crust and in the envelope of NSs, the magnetic field geometry drives the preferred direction for the heat conduction, acting in some regions as a thermal insulator.

In Viganò et al. (2013) (Paper I hereafter), we presented the most detailed 2D simulations of the magnetothermal evolution of isolated NSs to date, including updated microphysics inputs. We showed that the observed timing properties and bolometric luminosities of a varied sample of about 40 sources (including AXPs, SGRs, high-B radio pulsars, rotation-powered pulsars, X-ray isolated NSs, CCOs) can be accounted for by varying the strength of the initial poloidal field, and, in some cases, including the presence of a dominant toroidal field at birth.

In this paper, we extend our study of the NS zoo by studying the expected thermal spectra and pulse profiles predicted in a sample of magnetothermal evolutionary scenarios. In particular, we will contrast models with and without a dominant toroidal component of the magnetic field. Our results demonstrate that the thermal pulse profiles are markedly distinct in the two cases, hence allowing a probe of the magnetic field geometry.

We further address the issue of the magnitude of the blackbody radius and temperature inferred from fits to single blackbody models, when the underlying temperature profile is anisotropic.

Our paper is organized as follows: in § 2, we discuss the origin of the surface temperature anisotropy and show results from a set of simulations and ensuing surface temperature profiles. In § 3, we use the latter to build synthetic spectra, and compute the effective blackbody radius that would be inferred in fits; we also compute pulse profiles, for the same theoretical temperature profiles, in a soft X-ray thermal band. In § 4, we discuss our results in the context of observations. We summarize and conclude in § 5.

2 SURFACE TEMPERATURE PROFILES

The creation of surface temperature anisotropies in the crust and envelope of magnetised NSs has been extensively studied by different groups (Greenstein & Hartke 1983; Schaaf 1990; Heyl & Hernquist 2001; Potekhin & Yakovlev 2001; Geppert et al. 2004, 2006; Pérez-Azorín et al. 2006; Potekhin et al. 2007). In the outer ~ 100 m of a NS, the temperature gradient in the radial direction is very strong, with a typical drop of about two orders of magnitude. In the region where the magnetic field is radial (e.g., the poles), heat is efficiently transported along the radial direction, so that the surface is thermally connected to the inner crust and to the core. On the other hand, the regions with nearly tangential magnetic field (equatorial area for a dipolar field) are insulated and thermally disconnected from the hot core. Note, however, that 2D models have shown the importance of tangential heat conduction in limiting the anisotropy, compared with plane-parallel 1D models.

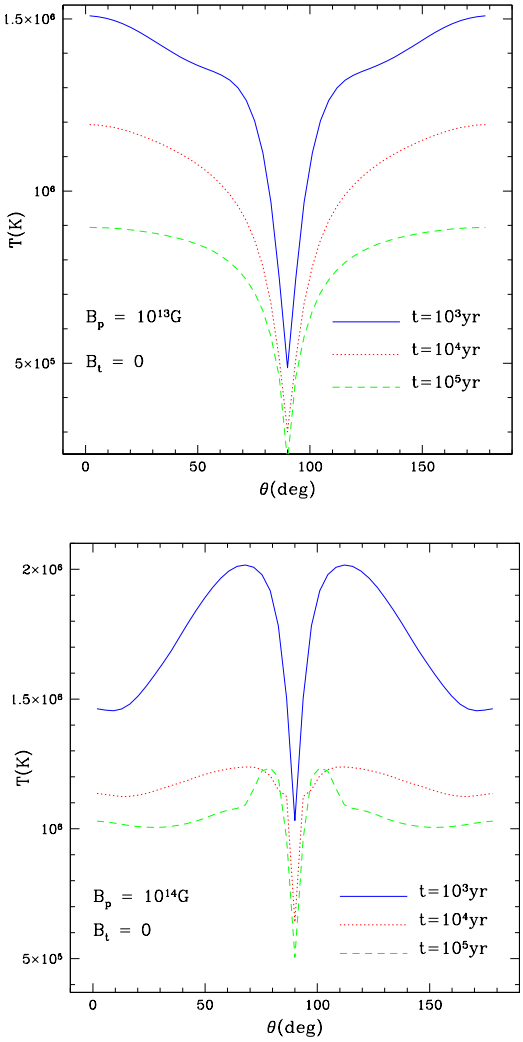

Figure 1. Temperature distribution on the surface of the NS, for models with a purely poloidal field at birth, and at different NS ages.

The degree of anisotropy is controlled by the ratio between thermal conductivity along and across the field lines, which in a classical (non-quantizing) approach can be approximated by

$$\frac{\kappa_\parallel}{\kappa_\perp} \approx 1 + (\omega_B \tau_e)^2 \qquad (1)$$

where $\omega_B = eB/m_e c$ and τ_e are the electron gyrofrequency and the electron relaxation time (the typical timescale between scattering processes suffered by electrons), respectively. Note that the classical approach is a good approximation only for weakly quantized matter (see e.g. Hernquist 1984). For magnetar-strength fields, quantum effects become important only at low density (the envelope) or low temperature, and the number of Landau levels must be consistently calculated. In our simulations, we use the full version of quantizing conductivities developed in the form of for-

tran codes by A. Potekhin (Potekhin 1999; Potekhin et al. 1999; Cassisi et al. 2007; Chugunov & Haensel 2007), which are available online[1].

At fixed temperature, transport across magnetic field lines is strongly suppressed for high magnetic field strengths, because $\omega_B \propto B$, and the anisotropy in the surface temperature is more pronounced. However, in some regimes, τ_e strongly depends on temperature, so that the so-called magnetization parameter $\omega_B \tau_e$ varies by several orders of magnitude during the evolution. In particular, at low temperatures, τ_e becomes large and anisotropy is expected even for weak magnetic fields (see the discussion in the final part of section 4 of Pons et al. 2009).

The general result for weak dipolar magnetic fields ($B \lesssim 10^{13}$ G) is that the magnetic poles are systematically hotter than the equatorial region. This situation can be inverted when internal heating sources are present. In Fig. 1, we show examples of the evolution of the surface temperature for different models parametrized by the magnetic field strength at the pole (B_p). The top panel shows results for an initially poloidal, strictly dipolar configuration, with $B_p = 10^{13}$ G. As the star becomes older, the magnetic field slowly dissipates but the temperature also decreases, and the surface temperature anisotropy in an old star can sometimes be larger than for a hot, young star with a higher magnetic field.

The particular temperature profile in the crust depends on the location of currents and where the dissipated magnetic energy is deposited. Eventually, an inversion of the angular temperature anisotropy in the crust can happen. However, this effect is filtered by the envelope: the blanketing effect of the envelope may reestablish the typical hot poles+cold equator profiles, depending on the strength of the magnetic field and temperature. In the bottom panel of Fig. 1, we show the evolution of the temperature for an initially poloidal, dipolar configuration, of strength $B_p = 10^{14}$ G. For young NSs, the poles are actually cooler than the tropical regions, and this counter-intuitive temperature profiles are kept for longer times for higher fields.

Note that, in the cases discussed above, the symmetry with respect to the equator is maintained throughout the evolution, due the initial choice of a purely poloidal, dipolar magnetic field. However, the magnetic field geometry is expected to be much more complicated, likely with the presence of strong internal components (toroidal field and poloidal multipoles). In order to explore the importance of a strong internal magnetic field, we show in Fig. 2 the temperature profiles for the same NS models as in Fig. 1, but with the addition of a strong toroidal component that contains over 90% of the magnetic energy.

During the evolution, the symmetry is broken due to the Hall term in the induction equation (see Paper I), which leads to a complex field geometry with asymmetric north and south hemispheres. The region with tangential field lines does not coincide with the equator, and asymmetric temperature profiles are expected. The degree of anisotropy strongly depends on the initial toroidal field strength, because of its insulating effect in the crust. In some cases, a

[1] http://www.ioffe.ru/astro/conduct (we use the 01.02.2013 version).

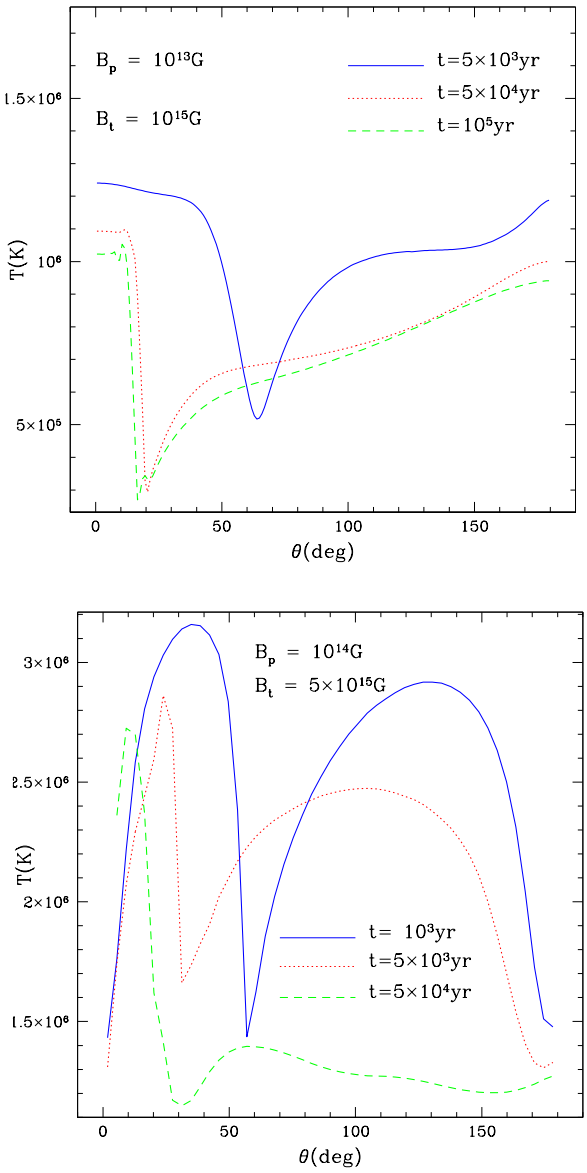

Figure 2. Temperature distribution on the surface of the NS, for models with an initial B field which has both a poloidal and a toroidal component.

configuration with radial field lines concentrated at small magnetic latitudes generates a step-like temperature profile (top panel, $t = 10^4, 10^5$ yr), with a sharp hot spot of $\sim 15 - 20°$. For a given initial magnetic field configuration at birth, the degree of anisotropy further increases with the age of the star.

In this paper we assume blackbody emission from the surface, without exploring other possible emission models, such as (magnetized) atmospheres and a condensed surface. We point out that, under the presence of a light-element atmosphere, the emerging spectrum would get distorted and, when fitted by a blackbody model, the inferred effective temperatures would be a factor $\sim 1.5 - 2$ larger (the so-called color-correction factor, e.g. Suleimanov et al. 2011), and, consequently, the inferred radius would be smaller. However, the emission model would barely affect the temperature anisotropy. Furthermore, note that a magnetic atmosphere

is expected to result in beaming of the outgoing radiation and could affect the observed pulse profiles, as widely discussed in the literature (e.g. Özel et al. 2001; Lloyd 2003; van Adelsberg & Lai 2006; Ho et al. 2007). Since here we are specifically interested in studying the anisotropy effects (both on spectra and pulse profiles) caused by the presence of a crustal field, we work under the assumption of local isotropic emission, and briefly discuss further possible modifications induced by an atmosphere. In the following, we compute spectra and pulse profiles for the temperature distributions of our models.

3 SPECTRA AND PULSE PROFILES.

The calculation of the phase-dependent emission from an extended region on the NS surface follows a well established formalism in the literature (Pechenick et al. 1983; Page 1995; Pavlov & Zavlin 2000). In the following, we use the same notation as in Perna et al. (2012). We define the time-dependent rotational phase $\gamma(t)$ as the azimuthal angle subtended by the magnetic dipole vector $\boldsymbol{\mu}$ around the axis of rotation. It is related to the modulus of the NS angular velocity, $\Omega(t)$, by $\gamma(t) = \int \Omega(t) dt$. The coordinate system is chosen so that the observer is located along the z axis; the inclination angle of the rotation axis, $\hat{\boldsymbol{\Omega}}$, with respect to the line of sight is indicated by α_R, while the angle between the magnetic dipole vector and the rotation angle is denoted by α_M. Thus, the angle between $\boldsymbol{\mu}$ and the line of sight is given by

$$\cos\alpha(t) = \cos\alpha_R \cos\alpha_M + \sin\alpha_R \sin\alpha_M \cos\gamma(t). \quad (2)$$

Due to the strong gravitational field of the NS, the trajectories of photons are substantially deflected as they travel to the observer. A photon emitted at an angle δ with respect to the surface normal will reach the (far away) observer if emitted at a colatitude θ on the star surface, where the relation between θ and δ is given by the ray-tracing function,

$$\theta(\delta) = \int_0^{\frac{R_s}{2R}} du\, x \left[\left(1 - \frac{R_s}{R}\right) \left(\frac{R_s}{2R}\right)^2 - (1-2u)u^2x^2 \right]^{-\frac{1}{2}}, \quad (3)$$

where $x \equiv \sin\delta$, and $R_s \equiv 2GM/c^2$ is the Schwarzchild radius of a star of mass M and radius R. Due to the spacetime curvature close to the NS, an observer at infinity measures a larger NS radius, $R_\infty = R(1 - \frac{R_s}{R})^{-1/2}$.

In order to obtain the (phase-dependent) spectrum at the observer one needs to integrate the local emission over the entire observable surface. Including the effect of gravitational redshift of the emitted radiation, this integral takes the form

$$F(E_\infty, \alpha) = \frac{2\pi}{c^2\, h^3} \frac{R_\infty^2}{D^2} E_\infty^2 \int_0^1 2x dx \times \int_0^{2\pi} \frac{d\phi}{2\pi} I(\theta, \phi, E), \quad (4)$$

in units of photons cm^{-2} s^{-1} keV^{-1}. In the above equation, E_∞ is the energy as measured by the distant observer. This is related to the local photon energy at the stellar surface by $E_\infty = E(1 - \frac{R_s}{R})^{1/2}$. The function $I(\theta, \phi, E)$ describes the distribution of the local emission. For simplicity, here we assume blackbody radiation at the local $T(\theta, \phi)$. Therefore, the emission is locally isotropic. This assumption allows us to disentangle the effects on the light curve modulation due to the temperature anisotropy (which is what we are interested in), from those produced by atmospheric effects, which are known to alter, and generally enhance, the flux modulation, as mentioned earlier.

From Eq. (4), we can easily compute the phase-averaged spectrum as

$$F_{\rm ave}(E_\infty) = \frac{1}{2\pi} \int_0^{2\pi} F[E_\infty, \alpha(\gamma)]\, d\gamma, \quad (5)$$

as well as the pulse profile in a given (observed) energy band, $\{E_{1,\infty}, E_{2,\infty}\}$.

$$F(\gamma) = \int_{E_{1,\infty}}^{E_{2,\infty}} F[E_\infty, \alpha(\gamma)]\, dE_\infty. \quad (6)$$

The pulsed fraction is defined as

$$\mathrm{PF} = \frac{F_{\max}(\gamma) - F_{\min}(\gamma)}{F_{\max}(\gamma) + F_{\min}(\gamma)}, \quad (7)$$

where the phases corresponding to the maximum and minimum of the flux may vary depending on the temperature distribution on the NS surface, as well as on the chosen energy band. With the local thermal emission assumed to be blackbody, phase-averaged spectra are multitemperature blackbodies.

3.1 Synthetic spectra and blackbody fits

Before studying the effect of the temperature anisotropy on the observable pulse profiles, we wish to address another related question of great importance for the interpretation of observations: given a spectrum from a realistic temperature distribution, such as those displayed in Figs. 1 and 2, what are the NS radius and temperature that would be obtained with a blackbody fit to the thermal component, as routinely done?

To answer this question, we imported the phase-averaged spectra from the temperature distributions in Figs. 1, 2 into the fitting software `Xspec` (Arnaud 1996). Using the recently developed `flx2tab` function in the `HEASARC` package, v6.13, we created the `atable` models for each one of the spectra. With `Xspec`, we then simulated synthetic observed spectra, using *XMM-Newton*/EPIC-pn response matrices in the `fakeit` procedure. We simulated also the interstellar absorption, by means of the `phabs` photoelectric absorption model with the Anders & Grevesse (1989) abundances, and the Balucinska-Church & McCammon (1992) photoelectric cross-sections. For all the models we discuss in this paper, the normalization is fixed by assuming a distance of 1 kpc, and the exposure time of the simulated observation is chosen so that the total number of photon counts would be of $\approx$ 5000 counts, as typical of realistic observations. For each model, we simulated 1000 random realizations of the spectrum. Then, for each spectrum, we proceeded to the spectral analysis in the standard way. In real observations, other contributions (e.g. hard tails, non-thermal components from rotation) extend the energy range to higher energy, but here we focus on the thermal contribution alone. We fitted the simulated spectra with the model

Model	Age [kyr]	T_{eff} [eV]	T_{max} [eV]	χ^2	T_{bb} [eV]	R_{bb} [km]
B13	1	113	130	1.38	112±2	$11.9^{+0.6}_{-0.5}$
B13	10	87	103	0.86	93±1	9.9±0.4
B13	100	68	78	1.17	72±1	10.3±0.5
B14	1	158	172	1.09	162±1	10.8±0.1
B14	10	102	106	1.01	100±1	12.1±0.5
B14	100	93	105	0.96	95±1	11.0±0.4
B13t	5	87	107	0.94	92±1	$9.8^{+0.4}_{-0.3}$
B13t	50	66	94	1.19	75±1	$8.0^{+0.6}_{-0.5}$
B13t	100	63	90	1.26	71±1	$8.2^{+0.6}_{-0.5}$
B14t	1	234	272	1.10	241±3	10.5±0.3
B14t	5	201	255	1.11	203±3	11.0±0.3
B14t	50	122	246	1.56	156±4	$6.1^{+0.5}_{-0.3}$

Table 1. Mean and standard deviation of the parameters over 1000 Monte Carlo realizations of synthetic absorbed spectra ($N_h = 10^{21}$ cm^{-2}), fitted with the `Xspec` model `phabs(zashift*bbodyrad)`. The theoretical models are the ones displayed in Fig. 1 and 2, labeled by the value of $\log(B_p^0)$, where B_p^0 is the strength of the initial dipolar poloidal field. The physical radius of the NS is 11.6 km in all the models. The suffix 't' indicates whether the initial field is dominated by a strong toroidal component. The reported χ^2 represents the mean value over all the Monte Carlo realizations.

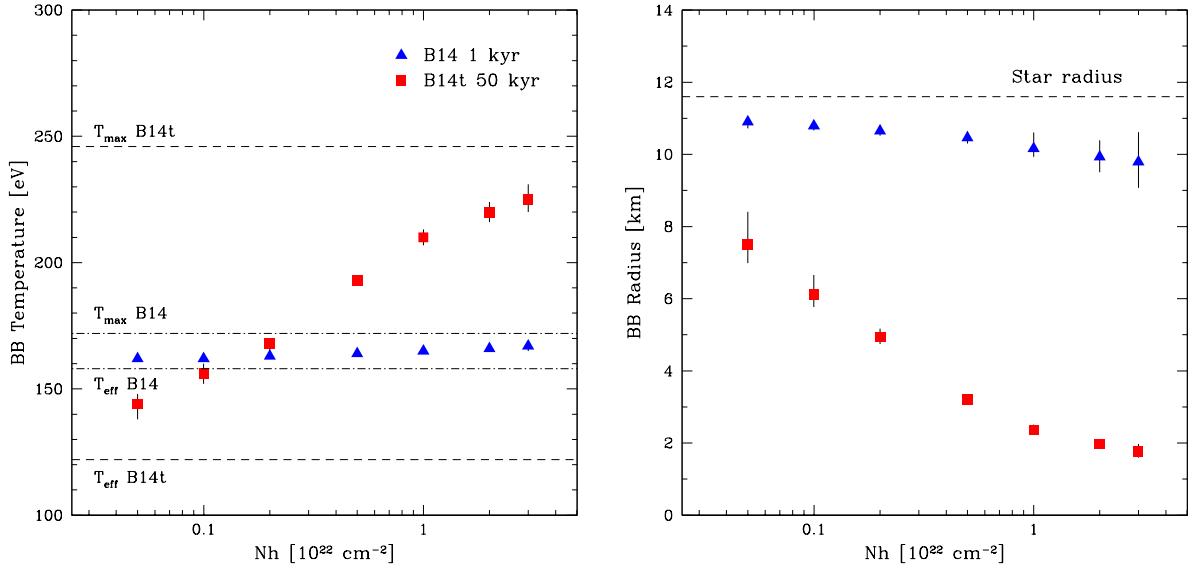

Figure 3. Dependence of temperature (left) and radius (right) on N_h, inferred by the best-fit `phabs(zashift*(bbodyrad))` model for two representative models: B14 at 1 kyr (blue triangles) and B14t at 50 kyr (red squares). Effective and maximum temperatures for both models are indicated as references. When a strong toroidal field is present (model B14t), the inferred BB temperatures and radii become a strong function of the interstellar absorption, unlike the case in which the field is purely poloidal (model B14).

`phabs(zashift*blackbody)`, where `zashift` applies the redshift correction, and `phabs` models the interstellar absorption. Our theoretical models for the temperature profiles and spectra were computed with $M = 1.4 M_\odot$ and $R = 11.6$ km (same NS model used in the simulations), yielding a redshift of $z = 0.25$.[2] We included an interstellar absorption of magnitude $N_h = 10^{21}$ cm^{-2}, which is typical of nearby sources. The results of the fits for all the models considered here are reported in Table 1. For the fitted parameters (T_{bb}, R_{bb}), we report the mean over the 1000 realizations, as as well the standard deviation.

In general, the temperature inferred by a single blackbody fit lies between the effective temperature $T_{\rm eff} \equiv (L_{\rm bol}/4\pi\sigma R^2)^{1/4}$ and the maximum temperature of the model, both shown in the table as well. By looking at the table and at the temperature profiles, we can roughly distinguish two kinds of models. In most models with a dominating poloidal magnetic field (B13, B14), the cold regions located near the equator have a small angular size and barely contribute to the total flux. Hence, the value of the inferred

[2] Note that, without redshift corrections, we would obtain exactly the same fit, but with temperature and radius at infinity, i.e. $T^\infty = T/(1+z)$ and $R^\infty = (1+z)R$.

radius is only slightly smaller than the star radius, and the temperature is only slightly higher than the effective temperature, which is not very different than the maximum temperature. On the other hand, when a strong toroidal component is present, the temperature profile, especially at old ages, can be roughly described by a cold component from a large part of the surface and a smaller, hot region. In these cases, the inferred BB radius (whereas a single BB provides a good fit to the thermal component) can be much smaller than the actual NS radius. The amount of reduction is, as it may be expected, a strong function of the energy-dependent absorption by the interstellar medium.

To study this effect, we analyzed in detail two representative models: B14 at 1 kyr and B14t at 50 kyr. For each of them, we generated synthetic spectra for values of absorption in the range $N_h \in [5 \times 10^{20}, 2 \times 10^{22}]$ cm^{-2}. Given the typical temperatures of our models, larger values of N_h would make the thermal emission from the source undetectable. In Fig. 3, we show the dependence of the best-fit blackbody parameters (radius and temperature) on N_h for both models. For the B14 model at 1 kyr (blue triangles), the best-fit temperatures and radii are almost independent of N_h, with only a slight overestimation of temperature (and underestimation of radius) for the strongest absorption. For $N_h \lesssim 10^{22}$ cm^{-2}, the inferred temperatures are within the 10% variability between the effective and maximum temperature, and the radius is compatible with, or a little smaller than the real radius. On the other hand, model B14t at 50 kyr (red squares) shows a large variability in the inferred temperature, caused by the large anisotropy and larger range of temperatures on the star surface. The inferred temperature tends to approach the highest temperature only for large absorption values, while it becomes lower as N_h decreases. The inferred radius of the emitting region is always significantly smaller than the real star radius, and can vary by up to a factor of four depending on the value of N_h, for the same model.

In Fig. 4 we show the simulated spectrum and the best-fit blackbody in one realization of the B14 model at 1 kyr, for two different values of the absorbing column density, $N_h = 10^{21}$ cm^{-2} and $N_h = 10^{22}$ cm^{-2}. In both cases, the single blackbody fit is acceptable and there is no evidence of anisotropy (i.e. need for additional components) in the spectrum.

For low values of absorption, the fake spectrum of model B14t at 50 kyr cannot be fitted accurately by a single blackbody. In the left panel of Fig. 5, we illustrate one realization for $N_h = 10^{21}$ cm^{-2}, which is not acceptable ($\chi^2 \sim 1.6$). In this case, a much better fit ($\chi^2 = 1.2$) is provided by two blackbodies with $kT_1 \simeq 90$ eV, $kT_2 \simeq 165$ eV, $R_2 \sim 5$ km, and R_1 compatible with the star radius, reflecting the real temperature profile. Larger values of absorption ($N_h = 10^{22}$ cm^{-2} in the right panel of Fig. 5) "hide" the cold component, so that the fit provides an estimate of the temperature and size of the hotter component, much smaller than the real radius. This explains the trend of Fig. 3 (right panel) with absorption: the larger the absorption, the hotter is the effective BB temperature measured from the fit, and hence the smaller is the inferred radius of the emitting region.

3.2 Pulse profiles

As evident from the discussion of the previous section, spectral modeling is generally degenerate: when the resolution is not extremely high, several models often fit equally well the same spectrum. This has been especially demonstrated by the results in Table 1: while the intrinsic spectra are composite blackbodies with a variety of temperature profiles, the resulting spectra can generally be fit by a single blackbody. A much deeper probe of the intrinsic temperature profile of the NS surface is provided by the pulse profile $F(\gamma)$ (cfr Eq.6) of the star in a thermal energy band. This is displayed in Figs. 6 and 7 for the set of models presented in Figs. 1 and 2. Fluxes are integrated over the typical soft X-ray [0.5-2] keV band. While the thermal flux generally dominates at lower energies, in practice, a combination of typical instrumental sensitivity and high interstellar absorption makes this band more relevant for comparison with observations. Note that the observed pulse profiles depend on the viewing angle (parametrized by α_M and α_R); here we consider, as our base model, the simplest geometry with $\alpha_R = \alpha_M = 90^\circ$ (orthogonal rotator). For this configuration, the viewing angle α becomes equal to the phase angle γ.

Some general features can be immediately inferred from inspection of Figs. 6 and 7. When the field is purely poloidal and hence the temperature profile is symmetric with respect to the equator (cfr. Fig. 1), the pulse profile is double peaked (Fig. 6). However, the maximum of the emission may or may not coincide with the sweeping of the axis of the magnetic dipole across the line of sight. This is a consequence of the fact that, for moderate strengths of the poloidal field, the temperature is higher at the poles (top panel of Fig. 1, $B_p = 10^{13}$ G), hence resulting in a flux maximum corresponding at $\gamma = 0$, while for stronger fields (bottom panel of Fig. 1), the hotter regions shift at intermediate latitudes on the NS surface, hence producing a maximum of the pulsation at large viewing angles.

A common feature of all the models with poloidal field alone (assumed purely dipolar) is that the pulsed fraction is very low; for a local isotropic photon distribution as assumed in Fig. 6, it remains constrained to within a few percent. This is the maximum that can be obtained without other effects, since we have considered an orthogonal rotator, which maximizes the flux variations. For geometrical configurations with α_R and/or α_M smaller than 90°, pulsed profiles become asymmetrical, and the pulsed fraction becomes even smaller. However, there are a number of effects which can increase the magnitude of the pulsed flux.

Firstly, high interstellar absorption, by preferentially absorbing low energy photons with respect to the high energy ones (more pulsed for BB emission), tends to increase the overall pulsed fraction of the thermal component in a wide energy band. To estimate the magnitude of the effect, we ran a few simulations with a column density $N_H = 10^{22}$ cm^{-2}, and using the absorption cross sections by Morrison & McCammon (1983). For a typical case with $B_p = 10^{13}$ G and $t = 10^4$ yr, we found that the amplitude of the pulsed fraction increased from 3.5% to 6.1% in the 0.5-2 keV band. Other (purely poloidal) cases are similar. A larger increase in the modulation can be typically obtained when considering wider energy bands (e.g. 0.05-10 keV), or

[ht]

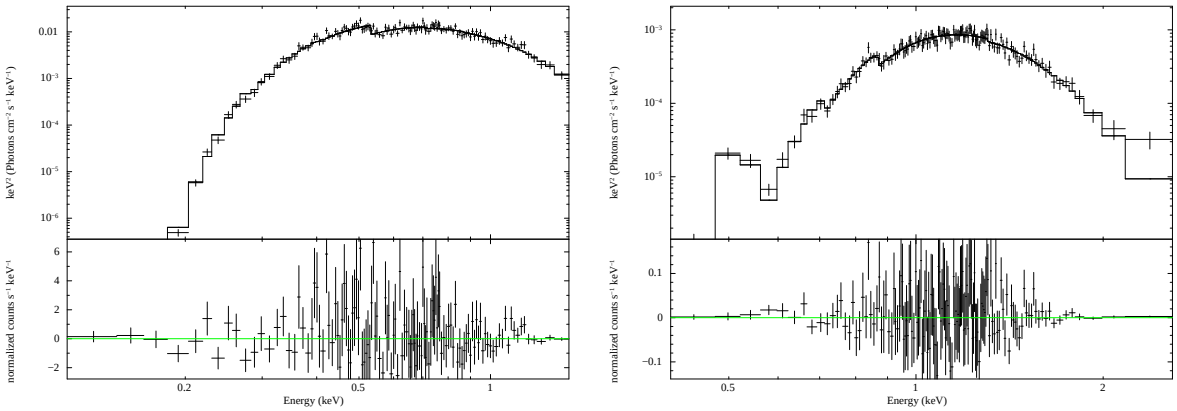

Figure 4. Synthetic spectra and best-fit blackbody model and residuals for the B14 model at 1 kyr, with $N_h = 10^{21}$ cm^{-2} (left panel) and $N_h = 10^{22}$ cm^{-2} (right).

[ht]

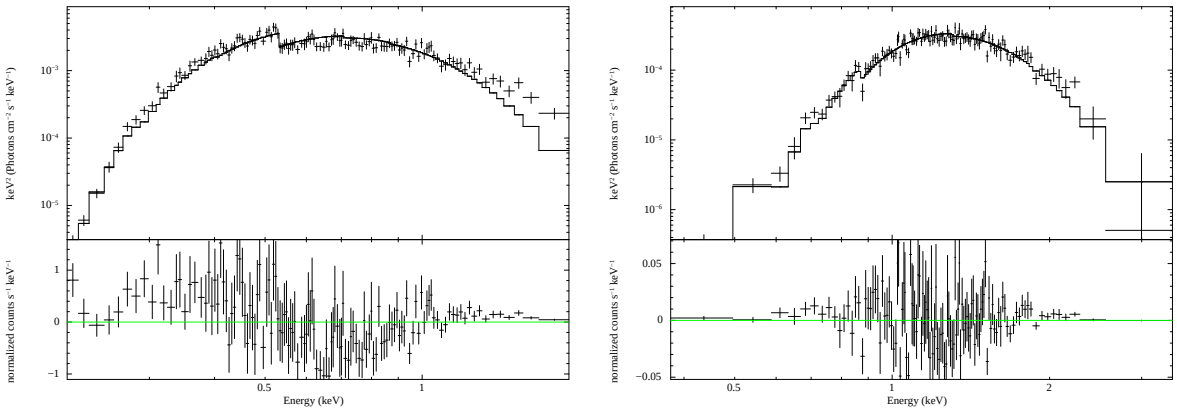

Figure 5. Synthetic spectra and best-fit blackbody model and residuals for the B14t model at 50 kyr, with $N_h = 10^{21}$ cm^{-2} (left panel) and $N_h = 10^{22}$ cm^{-2} (right).

larger absorbing column densities, as extensively discussed in Perna et al. (2000). However, for typical observational energy bands and absorbing columns, the PF of models with a mainly dipolar poloidal field remains small.

A more significant influence on the flux modulation derives from anisotropy in the local emission (see e.g. the parametric study by DeDeo et al. 2001). Magnetized atmospheres are known to create anisotropic radiation patterns (e.g. van Adelsberg & Lai 2006; Ho et al. 2008). A detailed computation of lightcurves with realistic, magnetized atmosphere profiles is beyond the scope of this work, as it would require a large number of atmosphere models, each for a certain temperature and varying magnetic field inclination over the surface of the star. Atmosphere models with inclined fields (Pavlov et al. 1994; Zavlin et al. 1995; Lloyd 2003; Ho 2007) are computationally very expensive[3]. Hence, following a number of previous investigations (Perna et al. 2000; DeDeo et al. 2001; Perna & Gotthelf 2008), we consider a parametrized form for the local radiation beaming, which we implement numerically by weighing the intensity I in Eq. (4) by a function $f(\delta)$, where δ is the angle between the normal to the surface and the direction of photon propagation. Note that, in realistic models of magnetized atmospheres, the shape of the radiation beam is a function of $B, E, T_{\rm eff}$. For magnetic fields normal to the NS surface, van Adelsberg & Lai (2006) find that there is a narrow pencil beam centered around the B field direction, accompanied by a broader fan beam at larger angles. However, for magnetar-level fields, and with the inclusion of vacuum polarization effects, the gap between the two beams is reduced, and the radiation emerges as a broad, featureless pencil beam centered along the B field direction. For inclined B fields, the pencil component of the beam still follows the direction of the field (e.g. Pavlov et al. 1994; Zavlin et al. 1995; Ho 2007).

In the following, with the purpose of simply providing an indication of the effect of a local anisotropic emission on the observed PFs of a purely dipolar, poloidal magnetic field configuration, we assume pencil beaming from a magnetic field normal to the surface, which we model as $f(\delta) \propto \cos^n \delta$, and we report the value of the PFs from pulse profiles computed with a beaming intensity $n = 1$. We again focus on the 0.5-2 keV band and, for each temperature distribution of Fig. 1, we report below the results for the model at the time t at which the PF is the highest (best scenario for ob-

[3] An approximate method for computing spectra and light curves with arbitrary temperatures and magnetic fields has been developed by Shabaltas & Lai (2012).

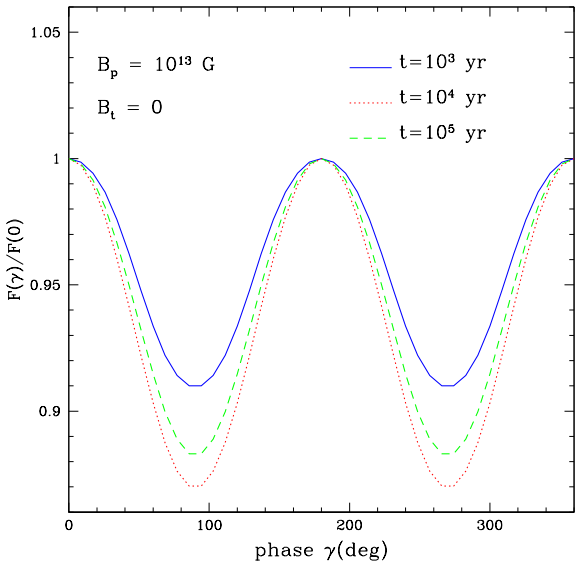

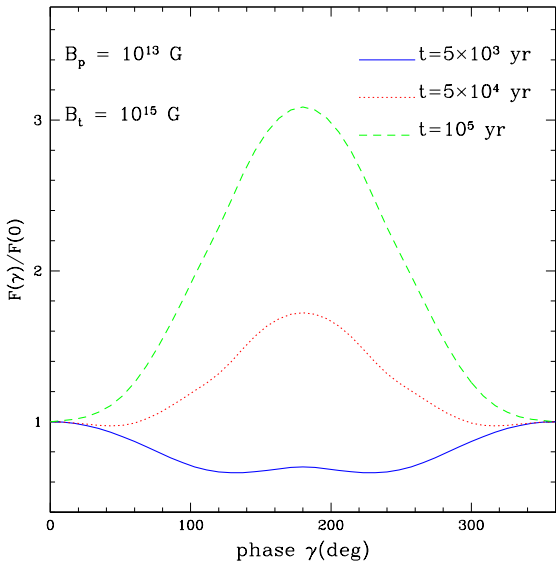

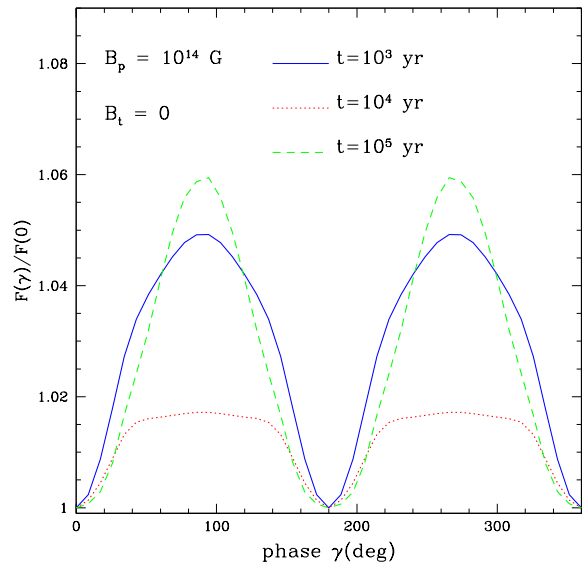

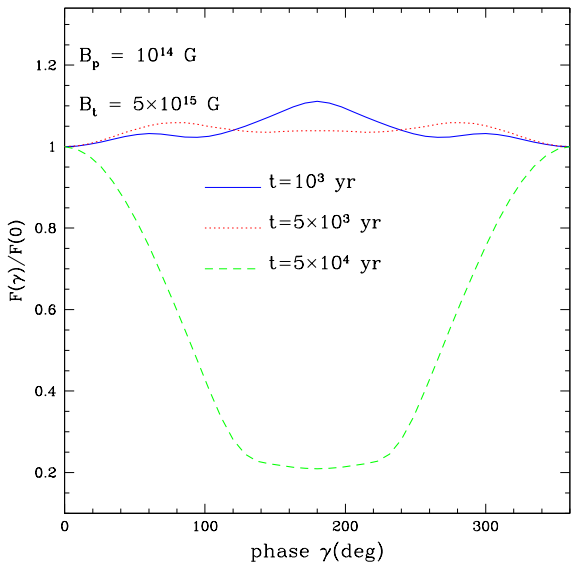

Figure 6. Pulse profiles in the 0.5-2 keV band for the temperature profiles of Fig. 1.

Figure 7. Pulse profiles in the 0.5-2 keV band for the temperature profiles of Fig. 2.

taining a highly modulated flux). We found that the PF of the $B_p = 10^{13}$ G, $t = 10^4$ yr model, increases from the 6.9% value of the isotropic case to 25% of the $n = 1$ case. In the case with $B_p = 10^{14}$ G, $t = 10^5$ yr, the PF increases from 2.8% to 12.2%. Clearly, a more extreme beaming of the local radiation would further increase the PF (DeDeo et al. 2001; Perna et al. 2000). Overall, our results show that a predominantly poloidal (dipolar) field results in double peaked profiles with a low level of flux modulation, unless the local emission is highly anisotropic.

These considerations change dramatically when the field has a strong large-scale toroidal component. The evolution of an initially strong toroidal, dipolar field breaks the symmetry of the temperature profile with respect to the equator (cfr. Fig. 2); an interesting consequence is that the resulting light curve becomes *single peaked*, and the pulsed fraction is much higher, reaching over 50% in the 0.5-2 keV band for some of the models (see Fig. 7). This is a particularly important result: without appealing to magnetospheric or beaming effects, purely thermal models *can* explain large pulsed fractions and single pulse profiles observed in a number of isolated NSs. We stress that this effect is achieved if the magnetic field has a strong large-scale component tangential to the surface (e.g., in the polar or azimuthal direction), which acts as an insulator for a large fraction of the surface. Other models, with high multipolar components, yield more complicated temperature profiles, with multiple small cold and hot regions. The resulting pulsed fraction, which averages out the small-scale differences, is small.

4 DISCUSSION

As our simulations show, the surface temperature (and hence the X-ray pulsed profile) of a NS changes dramatically with its initial field strength and topology, as well as its age.

The theoretical spectra and pulse profiles presented in the previous section bear direct implications for the observations of X-ray emission from isolated NSs. A direct comparison between our numerical results and X-ray spectra and pulse profiles of specific objects cannot be made unless the simulations are specifically tailored to particular objects, which is beyond the scope of this work. Hence, in the following, we will discuss some general features within the context of our findings.

4.1 Magnetars.

Magnetar spectra in the 0.3-10 keV energy range are typically best fit by the combination of a blackbody and a powerlaw. The thermal component, which often dominates in the lowest energy band, can be generally accounted for by a single BB; the inferred emission regions (for the best estimated distances) are most often found to be smaller than the whole surface of the NS. In fact, the small emitting radii appeared to argue in favor of alternative models, such as accretion from a fallback disk (e.g. Chatterjee et al. 2000), despite being ameliorated by fits with atmosphere models rather than pure BB ones (Perna et al. 2001).

Our magnetothermal models have shown that certain magnetic configurations (and especially some of those with a strong large-scale toroidal component) can result in inferred radii apparently incompatible with emission from the entire surface of the star when fitted with a pure blackbody, without atmospheric corrections. In particular, among the examples of theoretical models presented here, the one indicated with B14t at 50 kyr is especially illustrative. At small or moderate levels of interstellar absorption ($N_h \lesssim 5 \times 10^{21}$ cm^{-2}), this model is best fit by a two-blackbody: one cooler component consistent with emission from the entire surface of the star, and a hotter component with a smaller radius of the emitting region (~ 5 km). However, for more significant values of interstellar absorption ($N_h \gtrsim 10^{22}$ cm^{-1}), the cooler component is hidden, and then the NS appears as emitting only from a single, small, 'hot spot' of about 1-2 km in size (see also results by Shabaltas & Lai (2012) with analytical profiles for the magnetic field). This is indeed often the case for magnetars which, interestingly, have absorption column densities that typically exceed $\sim 10^{22}$ cm^{-2} (Esposito et al. 2008; Rea et al. 2005; Gelfand & Gaensler 2007).

Thermal pulsed profiles of magnetars display a mixed morphology. A notable example of a (almost symmetric) double peaked light curve is the magnetar 1E 2259+586 (Patel et al. 2001; Woods et al. 2004). A double peaked profile could be obtained with an initial poloidal, dipolar field, and a toroidal, quadrupolar configuration. However, the high PF at about the 20% level of the thermal flux could only be accounted for by a significant anisotropy in the local emission ($f(\delta) \propto \cos^{1.5}\delta$ in the notation of § 3). Another double peaked magnetar is 4U 0142+0162; the low level of modulation of this object (around the 10% level) does not constitute a problem for symmetric temperature profiles (Rea et al. 2007). Also for this object, the dominant toroidal component would have to be of even parity in order not to break the symmetry with respect to the equator.

For most other magnetars, on the other hand, the pulsed thermal (quiescent) component is single peaked and often highly pulsed. Examples are[4] (among others) 1E 1048.1-5937 (Tam et al. 2008), XTE J1810-197 (Bernardini et al. 2009, 2011), 1E 1207.4-5209 (Halpern & Gotthelf 2011), 1E 1547.0-5408 (Dib et al. 2012), SGR 0418+5729 (Rea et al. 2013), SGR J1822.3-1606 (Rea et al. 2012). The single peaked, highly modulated flux is generally associated to emitting areas that are much smaller than the entire surface of the NS. Single peaks coupled with a large PF rule out symmetrical emission geometries with small angles α_R and/or α_M. They rather imply a temperature distribution on the surface of the star which is asymmetric with respect to the equator.

Our results hence suggest that, for these objects, a strong toroidal component must be present in the interior of the star. We note that, in particular for the case of the low-B magnetars SGR 0418+5729 and SGR J1822.3-1606, a strong internal field has been invoked for the objects to have a non-negligible probability of an outburst (Rea et al. 2012, 2013). More generally, it has been discussed (Perna & Pons 2011; Pons & Perna 2011; Paper I) how a strong internal toroidal field is more likely to make a NS to appear as a magnetar (i.e. higher thermal luminosity, higher outburst frequency) as compared to a NS with a similar dipolar field but insignificant toroidal composnent. Our findings about the shape of the pulse profiles, as well as on the sizes of the inferred blackbody radii, provide an additional support to the earlier suggestions.

We note, however, that tiny spots (a fraction of km in size), such as, for example, the one measured for the thermal emission of CXO J164710.2-455216 (Muno et al. 2006; Skinner et al. 2006; Israel et al. 2007) would be hard to explain with anisotropic, internal heat alone. Such intensely heated, very small regions are more likely to result from currents in a twisted magnetic bundle (Beloborodov 2009; Turolla et al. 2011).

4.2 The magnificent seven.

Another class of objects for which our results are of direct relevance is that of the X-ray Isolated Neutron Stars (XINSs, also known as the "Magnificent Seven", and first discovered by Walter et al. 1996). These are characterized by purely thermal spectra, blackbody radii of a few km in size, and generally modest pulsation levels, ranging from a few percent to 18%. These objects, with inferred dipolar fields in the few $\times 10^{13}$ G range, have timing properties and X-ray luminosities consistent with those of evolved magnetars[5] (for a review of their properties see e.g. Trümper 2005; Turolla 2009), i.e. stars born with dipolar fields of a few 10^{14} G, which decayed to the current value within a few $\times 10^5$ years

[4] In the quoted references, when the thermal band is not explicitly separated, we simply refer at the pulsed profile in the lowest energy band.

[5] The birthrates of magnetars and of XINSs have been computed by a number of authors (Gill & Heyl 2007; Keane & Kramer 2008; Ferrario & Wickramasinghe 2008; Popov et al. 2010); however, the inferred numbers are still rather uncertain due to small number statistics and the recent discovery of low field magnetars (Rea et al. 2010), as well as of transient magnetars (Ibrahim et al. 2004).

(see Paper I for a thorough description of the coupled evolution of magnetic field and temperature). The observed pulse profiles are close to sinusoidal, and single-peaked except for RX J1308.6+2127, which is double-peaked.

Consistently with previous work (Page 1995), which used simplified, analytical models for the dipolar temperature distribution, we find that single peaked profiles from purely dipolar, poloidal fields can only be produced for a small range of oblique viewing geometries and, when so, they would yield very low PFs, typically not exceeding a few percent if the local emission is purely isotropic. Anisotropic emission can largely increase the PF as discussed in Sec 3.2, and previous work (Zane & Turolla 2006) has shown that it is possible to fit reasonably well the pulsed profiles of these objects with a combination of Hydrogen atmospheric models, and a star-centred dipole plus a quadrupole topology.

4.3 Central Compact Objects.

Last, we conclude with the discussion of another class of isolated NSs whose observational properties can be interpreted within the context of our findings – that is the sample of objects known as central compact objects or CCOs. These relatively young objects (often still found at the center of their supernova remnant) are characterized by a low inferred external (dipolar) field, generally $B_p \lesssim 10^{11}$ G, which is at odd with the hints for anisotropic distribution of temperature inferred from the analysis of their pulse profiles. For example, 1E 1207.4-5209, which displays a single, rather symmetric pulse profile in the 0.5-2.5 keV band (see Fig. 13 in Gotthelf et al. 2013), has a PF of about 10%. PSR J1852+0040 (Halpern & Gotthelf 2010) also displays a single peak and a very large pulsed fraction of 64%, clearly problematic for the CCOs. These puzzling observations have called into question the presence of a strong internal toroidal field (Halpern & Gotthelf 2010; Shabaltas & Lai 2012; Viganò & Pons 2012). Our findings of § 3 support this suggestion. We have showed that high PFs, reaching 50-65% for some particular cases with strong B_t, can be achieved, and correlate with a single thermal peak, as well as with a smaller inferred BB radius. In particular, we can consider again as a qualitative representative example (since the simulations are not tailored to specific objects) model B14t at 50 kyr. This has a PF of 66% and a BB radius $\lesssim 3$ km for $N_h \gtrsim 5 \times 10^{21}$ cm^{-2}, as shown in Fig. 3. Note that the presence of an atmospheric color correction factor (not included in our modeling) would make this emitting region to appear even smaller, hence further ameliorating the issue of the small emitting areas seen in some of these objects (such as PSR J1852+0040 indeed, Halpern & Gotthelf 2010).

The CCO PSR J0821-4300 in Puppis A also displays a clear single peak in the thermal component. However, phase-resolved spectroscopy shows that the 0.5-1 keV pulsed flux is offset by half a phase cycle with respect to the 1.5-4.5 keV band (Gotthelf & Halpern 2009). Detailed modeling by Gotthelf et al. (2010) showed that two well separated, antipodal regions of different sizes and temperatures can closely match the observations. As discussed above, such a strong temperature anisotropy must imply a strong internal magnetic component, which contrasts the low inferred dipolar field of about 10^{11} G (Gotthelf et al. 2013). At a qualitative level, we note that a temperature profile similar to that of model B14t at age $t = 5 \times 10^4$ yr has some key features that could mimic what observed for this object. At phase $\gamma = 0$, the emission from this object is in fact dominated by the hot, compact region at $\theta \lesssim 20^\circ$, and would hence appear as a small hot spot. On the other hand, when the star is at phase $\gamma = 180^\circ$, only the cooler, more extended region that covers the star for $\theta \gtrsim 80^\circ$ (cfr. bottom panel of Fig. 2, dashed line) is visible to the observer. The effective flux to the observer would mimic that of two antipodal regions, of different temperatures. We reserve to future work a more comprehensive exploration of initial magnetic field configurations that can yield special temperature anisotropy patterns tailored to specific objects.

5 SUMMARY

We have used results from detailed simulations of the magnetothermal evolution of isolated NSs to explore the temperature maps, and the resulting spectra and pulse profiles, at different NS ages, for a variety of magnetic field configurations and strengths. In particular, we contrasted models with a purely poloidal (dipolar) field at birth, with cases in which the initial magnetic field is dominated by a strong toroidal dipolar component ($\gtrsim 90\%$ of magnetic energy stored in the toroidal field). Intermediate cases, where $\lesssim 50\%$ of magnetic energy is stored in the toroidal field, are very similar to the case with an initial purely poloidal field.

We have found that poloidal-dominated configurations can only yield symmetric pulse profiles (as expected, for a wide range of viewing geometries) and very low pulsed fractions unless the local emission is highly beamed. On the other hand, the anisotropies in the surface temperature profile induced by the presence of a strong, large-scale toroidal field generally produce single pulsed profiles, with a pulsed fraction that can reach the 50-60% level even for purely isotropic local emission. These results are particularly relevant to the interpretation of the thermal spectra of magnetars, which are often single peaked and highly pulsed. A strong internal component is in fact believed to play an important role in enhancing their X-ray luminosities, and in producing a non-negligible outburst rate, even in 'low field' magnetars. Another class of objects for which our results bear direct relevance is that of the CCOs. Although their inferred external (dipolar) fields are very low, some of them present strong hints for a strong surface temperature anisotropy. Representative cases from our simulations display a qualitative behaviour consistent with the observational properties of these objects.

Another finding of our work is that the theoretical thermal X-ray spectra, when simulated as "real" spectra and then fitted with a single blackbody (as routinely done in spectral studies) yield blackbody radii which can be either comparable to, or smaller than, the actual NS radius, depending on the magnitude of the surface temperature anisotropy and the absorption column. Generally, older objects are more anisotropic, and their inferred BB radii are smaller. A strong large-scale toroidal field further increases the surface temperature anisotropy; this, coupled with strong interstellar absorption, can lead to 'measured' BB radii of $\sim$ 1-2 km in size. This is again of high relevance

for the interpretation of X-ray observations of isolated NSs, such as e.g. magnetars, which very often display blackbody radii of only a few km in size.

As a further related consequence, caution should be exercised when using the radius derived from spectral fitting, in combination with a mass or redshift measurement, to constrain the properties of the equation of state of dense matter. Even for objects with a measured low external magnetic field, a strong internal component can exist, and hence influence the delicate measurement of the size of the emitting region.

ACKNOWLEDGEMENTS

This research was supported by NSF grant No. AST 1009396 and NASA grants AR1-12003X, DD1-12053X, GO2-13068X, GO2-13076X (RP), grants AYA 2010-21097-C03-02 (DV, JAP), AYA2009-07391, AYA2012-39303, SGR2009-811, and iLINK 2011-0303 (NR). DV is supported by a fellowship from the *Prometeo* program for research groups of excellence of the Generalitat Valenciana (Prometeo/2009/103) and NR is supported by a Ramon y Cajal Fellowship. DV thanks JILA (Boulder, CO, USA) for its kind hospitality during the time that some of this work was carried out. Last, we thank an anonymous referee for very helpful comments.

REFERENCES

Aguilera D. N., Pons J. A., Miralles J. A., 2008, A&A, 486, 255
Anders E., Grevesse N., 1989, Geochim. Cosmochim. Acta, 53, 197
Arnaud K. A., 1996, in Jacoby G. H., Barnes J., eds, Astronomical Data Analysis Software and Systems V Vol. 101 of Astronomical Society of the Pacific Conference Series, XSPEC: The First Ten Years. p. 17
Balucinska-Church M., McCammon D., 1992, ApJ, 400, 699
Beloborodov A. M., 2009, ApJ, 703, 1044
Bernal C. G., Lee W. H., Page D., 2010, RMAA, 46, 309
Bernardini F., Israel G. L., Dall'Osso S., Stella L., Rea N., Zane S., Turolla R., Perna R., Falanga M., Campana S., Götz D., Mereghetti S., Tiengo A., 2009, A&A, 498, 195
Bernardini F., Perna R., Gotthelf E. V., Israel G. L., Rea N., Stella L., 2011, MNRAS, 418, 638
Cassisi S., Potekhin A. Y., Pietrinferni A., Catelan M., Salaris M., 2007, ApJ, 661, 1094
Chatterjee P., Hernquist L., Narayan R., 2000, ApJ, 534, 373
Chugunov A. I., Haensel P., 2007, MNRAS, 381, 1143
DeDeo S., Psaltis D., Narayan R., 2001, ApJ, 559, 346
Dib R., Kaspi V. M., Scholz P., Gavriil F. P., 2012, ApJ, 748, 3
Esposito P., Israel G. L., Zane S., Senziani F., Starling R. L. C., Rea N., Palmer D. M., Gehrels N., Tiengo A., de Luca A., Götz D., 2008, MNRAS, 390, L34
Ferrario L., Wickramasinghe D., 2008, MNRAS, 389, L66
Gelfand J. D., Gaensler B. M., 2007, ApJ, 667, 1111
Geppert U., Küker M., Page D., 2004, A&A, 426, 267
Geppert U., Küker M., Page D., 2006, A&A, 457, 937
Gill R., Heyl J., 2007, MNRAS, 381, 52
Gotthelf E. V., Halpern J. P., 2009, ApJL, 695, L35
Gotthelf E. V., Halpern J. P., Alford J., 2013, ArXiv e-prints
Gotthelf E. V., Perna R., Halpern J. P., 2010, ApJ, 724, 1316
Greenstein G., Hartke G. J., 1983, ApJ, 271, 283
Halpern J. P., Gotthelf E. V., 2010, ApJ, 709, 436
Halpern J. P., Gotthelf E. V., 2011, ApJL, 733, L28
Hernquist L., 1984, ApJS, 56, 325
Heyl J. S., Hernquist L., 2001, MNRAS, 324, 292
Heyl J. S., Kulkarni S. R., 1998, ApJL, 506, L61
Ho W. C. G., 2007, MNRAS, 380, 71
Ho W. C. G., 2011, MNRAS, 414, 2567
Ho W. C. G., Kaplan D. L., Chang P., van Adelsberg M., Potekhin A. Y., 2007, MNRAS, 375, 821
Ho W. C. G., Potekhin A. Y., Chabrier G., 2008, ApJS, 178, 102
Ibrahim A. I., Markwardt C. B., Swank J. H., Ransom S., Roberts M., Kaspi V., Woods P. M., Safi-Harb S., Balman S., Parke W. C., Kouveliotou C. andHurley K., Cline T., 2004, ApJL, 609, L21
Israel G. L., Campana S., Dall'Osso S., Muno M. P., Cummings J., Perna R., Stella L., 2007, ApJ, 664, 448
Keane E. F., Kramer M., 2008, MNRAS, 391, 2009
Lloyd D. A., 2003, PhD thesis, HARVARD UNIVERSITY
Morrison R., McCammon D., 1983, ApJ, 270, 119
Muno M. P., Clark J. S., Crowther P. A., Dougherty S. M., de Grijs R., Law C., McMillan S. L. W., Morris M. R., Negueruela I., Pooley D., Portegies Zwart S., Yusef-Zadeh F., 2006, ApJL, 636, L41
Muslimov A., Page D., 1995, ApJL, 440, L77
Özel F., Psaltis D., Kaspi V. M., 2001, ApJ, 563, 255
Page D., 1995, ApJ, 442, 273
Patel S. K., Kouveliotou C., Woods P. M., Tennant A. F., Weisskopf M. C., Finger M. H., Göğüş E., van der Klis M., Belloni T., 2001, ApJL, 563, L45
Pavlov G. G., Shibanov Y. A., Ventura J., Zavlin V. E., 1994, A&A, 289, 837
Pavlov G. G., Zavlin V. E., 2000, ApJ, 529, 1011
Pechenick K. R., Ftaclas C., Cohen J. M., 1983, ApJ, 274, 846
Pérez-Azorín J. F., Miralles J. A., Pons J. A., 2006, A&A, 451, 1009
Perna R., Gotthelf E. V., 2008, ApJ, 681, 522
Perna R., Heyl J., Hernquist L., 2000, ApJL, 538, L159
Perna R., Heyl J. S., Hernquist L. E., Juett A. M., Chakrabarty D., 2001, ApJ, 557, 18
Perna R., Ho W. C. G., Verde L., van Adelsberg M., Jimenez R., 2012, ApJ, 748, 116
Perna R., Pons J. A., 2011, ApJL, 727, L51
Pons J. A., Miralles J. A., Geppert U., 2009, A&A, 496, 207
Pons J. A., Pérez-Azorín J. F., Miralles J. A., Miniutti G., 2007, Ap&SS, 308, 247
Pons J. A., Perna R., 2011, ApJ, 741, 123
Popov S. B., Pons J. A., Miralles J. A., Boldin P. A., Posselt B., 2010, MNRAS, 401, 2675
Potekhin A. Y., 1999, A&A, 351, 787
Potekhin A. Y., Baiko D. A., Haensel P., Yakovlev D. G., 1999, A&A, 346, 345

Potekhin A. Y., Chabrier G., Yakovlev D. G., 2007, Ap&SS, 308, 353
Potekhin A. Y., Yakovlev D. G., 2001, A&A, 374, 213
Rea N., Esposito P., Turolla R., Israel G. L., Zane S., Stella L., Mereghetti S., Tiengo A., Götz D., Göğüş E., Kouveliotou C., 2010, Science, 330, 944
Rea N., Israel G. L., Esposito P., Pons J. A., Camero-Arranz A., Mignani R. P., Turolla R., Zane S., Burgay M., Possenti A., Campana S., Enoto T., Gehrels N., Göğüş E., Götz D., Kouveliotou C., Makishima K., 2012, ApJ, 754, 27
Rea N., Israel G. L., Pons J. A., Turolla R., Vigano D., Zane S., Esposito P., Perna R., Papitto A., Terreran G., Tiengo A., Salvetti D., Girart J. M., Palau A., Possenti A., Burgay M., Gogus E., Caliandro A., Kouveliotou C., 2013, ApJ, 770, 65
Rea N., Nichelli E., Israel G. L., Perna R., Oosterbroek T., Parmar A. N., Turolla R., Campana S., Stella L., Zane S., Angelini L., 2007, MNRAS, 381, 293
Rea N., Oosterbroek T., Zane S., Turolla R., Méndez M., Israel G. L., Stella L., Haberl F., 2005, MNRAS, 361, 710
Schaaf M. E., 1990, A&A, 227, 61
Shabaltas N., Lai D., 2012, ApJ, 748, 148
Skinner S. L., Perna R., Zhekov S. A., 2006, ApJ, 653, 587
Suleimanov V., Poutanen J., Werner K., 2011, A&A, 527, A139
Tam C. R., Gavriil F. P., Dib R., Kaspi V. M., Woods P. M., Bassa C., 2008, ApJ, 677, 503
Thompson C., Duncan R. C., 1995, MNRAS, 275, 255
Trümper J. E., 2005, in Baykal A., Yerli S. K., Inam S. C., Grebenev S., eds, NATO ASIB Proc. 210: The Electromagnetic Spectrum of Neutron Stars Observations of Cooling Neutron Stars. p. 117
Turolla R., 2009, in Becker W., ed., Astrophysics and Space Science Library Vol. 357 of Astrophysics and Space Science Library, Isolated Neutron Stars: The Challenge of Simplicity. p. 141
Turolla R., Zane S., Pons J. A., Esposito P., Rea N., 2011, ApJ, 740, 105
van Adelsberg M., Lai D., 2006, MNRAS, 373, 1495
Viganò D., Pons J. A., 2012, MNRAS, 425, 2487
Viganò D., Rea N., Pons J. A., Perna R., Aguilera D. N., Miralles J. A., 2013, ArXiv e-prints
Walter F. M., Wolk S. J., Neuhäuser R., 1996, Nat, 379, 233
Woods P. M., Kaspi V. M., Thompson C., Gavriil F. P., Marshall H. L., Chakrabarty D., Flanagan K., Heyl J., Hernquist L., 2004, ApJ, 605, 378
Young E. J., Chanmugam G., 1995, ApJL, 442, L53
Zane S., Turolla R., 2006, MNRAS, 366, 727
Zavlin V. E., Pavlov G. G., Shibanov Y. A., Ventura J., 1995, A&A, 297, 441